The role of intermolecular interactions in $[Fe(X\text{-}salEen)_2]ClO_4$ spin crossover complexes†

Marcos A. Bento,[a] Tiago Gomes,[a] Frederico F. Martins,[b] Adrià Gil,[b,c] Liliana P. Ferreira,[d,e] Sónia Barroso,‡[f,g] Clara S. B. Gomes,[h] Yann Garcia[i] and Paulo N. Martinho *[a]

Two new spin crossover (SCO) Fe(III) compounds were prepared, their structures were analysed and their magnetic properties were investigated. An exhaustive analysis of the effects of halogen substitution and aromatic ring functionalisation on the magnetic properties of non-solvated Fe(III) perchlorate complexes has been performed. Through comparative analysis, different magnetic profiles were found for the compounds studied, namely F (**1**), Cl (**2**), H (**3**), Br (**4a**, **4b**), and I (**5**). Using tools like Hirshfeld analysis, the study revealed patterns in octahedral distortions and deviations from the ideal octahedral geometry. The SCO phenomenon as the conducting wire in this study, emphasises the influence of intermolecular interactions on the low spin (LS) to high spin (HS) transitions in these halogen-substituted complexes. The prevalence of H···H contributions has been demonstrated, albeit being the weakest and an inverse strength relationship in H···X interactions ranging from F to I. The findings not only interpret the intricate balance between halogen substitution, functionalisation, and intermolecular interactions in modulating magnetic properties but also direct future works in designing similar molecular systems.

1. Introduction

In recent years, the focus of spin crossover (SCO) research has expanded beyond the core properties of individual complexes to, for example, understanding the influence of intermolecular interactions on their spin states.[1] While early studies primarily concentrated on intramolecular factors governing spin transitions, namely coordination sphere and ligand field strength,[2,3] it has become increasingly evident that intermolecular interactions play a crucial role in the cooperative behaviour and stability of SCO complexes in the solid state.[4–7] These interactions include hydrogen bonding,[8–11] π–π stacking,[12–15] halogen bonding,[16–19] and crystal packing effects,[20–23] which can drastically impact the thermodynamic and kinetic aspects of the SCO phenomenon.

Understanding the nature and effect of intermolecular interactions in SCO complexes is vital for tailoring their properties and optimising their performance when it comes to their applications. This knowledge can help in the design of new materials with enhanced SCO characteristics, including materials with higher thermal hysteresis, increased stability, and improved response to external stimuli.[24,25]

We recently reviewed the SCO topic with a focus on the influence of halogens as ligands or substituents in mono- and binuclear transition metal complexes, aiming to identify trends and correlations in properties associated with halogen substitution patterns. Alongside an in-depth examination of

[a]*Centro de Química Estrutural, Institute of Molecular Sciences, Departamento de Química e Bioquímica, Faculdade de Ciências, Universidade de Lisboa, Campo Grande, 1749-016 Lisboa, Portugal. E-mail: pnmartinho@ciencias.ulisboa.pt*

[b]*BioISI – Biosystems & Integrative Sciences Institute, Faculdade de Ciências, Universidade de Lisboa, Campo Grande, 1749-016 Lisboa, Portugal*

[c]*Departament de Química, Física i Ciències Ambientals i del Sòl, ETSEA – Escola Tècnica Superior d'Enginyeria Agrària, Universitat de Lleida, Av. de l'alcalde Rovira Roure, 191, E25198 Lleida, Catalunya, Spain*

[d]*Department of Physics, University of Coimbra, 3004-516 Coimbra, Portugal*

[e]*Centro de Física Teórica e Computacional, Faculdade de Ciências, Universidade de Lisboa, Campo Grande, Edifício C8, 1749-016 Lisboa, Portugal*

[f]*UCIBIO, Departamento de Química, Faculdade de Ciências e Tecnologia, Universidade NOVA de Lisboa, 2829-516 Caparica, Portugal*

[g]*i4HB, Faculdade de Ciências e Tecnologia, Universidade NOVA de Lisboa, 2829-516 Caparica, Portugal*

[h]*LAQV-REQUIMTE, Department of Chemistry, NOVA School of Science and Technology, NOVA University of Lisbon, 2829-516 Caparica, Portugal*

[i]*Institute of Condensed Matter and Nanosciences, Molecular Chemistry, Materials and Catalysis (IMCN/MOST), Université Catholique de Louvain, Place L. Pasteur 1, 1348 Louvain-la-Neuve, Belgium*

† Electronic supplementary information (ESI) available. CCDC 2310296–2310299. For ESI and crystallographic data in CIF or other electronic format see DOI: **https://doi.org/10.1039/d4dt00400k**

‡ Current address: MARE - Marine and Environmental Sciences Centre/ARNET - Aquatic Research Network, Polytechnic of Leiria, Cetemares, 2520-620 Peniche, Portugal

their properties, we explored structural characteristics and other relevant information. Additionally, we employed a simple model incorporating density functional theory (DFT) calculations to evaluate several parameters and establish potential correlations between calculated parameters and SCO data.[26]

Morgan *et al.* have dedicated a great part of their work on SCO in Mn(III) to understanding how intermolecular interactions affect this phenomenon for this metal ion and found that intermolecular interactions are normally affected by the transition between spin states and are more important and highly present for the LS state and normally absent in the HS state.[27–30]

Other authors have also studied the Fe(III) ion with both the qsal (qsal = *N*-(8-quinolyl)-salicylaldimine) and salEen (salEen = *N*-ethyl-*N*-(2-aminoethyl)-salicylaldiminate) ligands and found that intermolecular interactions are very important in the process of stabilisation of spin states and confer cooperativity on the compound.[31–36]

We previously reported the halide (Cl, Br, I) derivatives of [Fe(3,5-halide-salEen)$_2$]X (X = ClO_4^-, BPh_4^-) and tried to understand the origin of their interesting and unusual magnetic profiles.[34,35,37–40] For ClO_4^- salts, the bromine derivative was obtained in two polymorphic forms each with very distinct magnetic profiles, one exhibiting the thermosalient effect while changing the spin state and the other displaying abrupt spin transition at 172 K. The iodine derivative, in turn, behaved very similarly to one of the polymorphic forms of the bromine derivative and also displayed the thermosalient effect while changing the spin state. However, this behaviour was only found in the first heating/cooling cycle and after this, the magnetic profile of the compound was only gradual and matched the profile obtained for the cooling routine. Based on the results obtained for these two halides, we decided to extend our studies to the remaining halides, fluoride and chloride. With this study we tried to understand the effect of halide in unsolvated perchlorate salts of Fe(III) salEen derivatives and trends were extracted with the help of crystallography and Hirshfeld analysis.

2. Experimental section

2.1. General remarks

Caution: perchlorate salts are notorious for their explosiveness; thus, precautionary measures must be taken when handling them. *N*-Ethylethylenediamine, 5-fluorosalicylaldehyde, 5-chlorosalicylaldehyde, sodium perchlorate, iron(II) chloride and solvents were purchased and used without further purification. The preparation of Fe(III) complexes strategically starts from their Fe(II) salts as we experienced that by this method the likeliness to obtain unsolvated compounds is higher. IR spectra were recorded on a PerkinElmer FTIR spectrophotometer. Microanalyses (C, H and N) were measured using an elemental analysis service at the University of Vigo, Spain.

Magnetisation measurements as a function of temperature were performed using a SQUID magnetometer (Quantum Design MPMS). The curves were obtained at 1000 Oe for temperatures ranging from 10 to 370 K and the molar susceptibility (χ_M) values were corrected for diamagnetism.

Differential scanning calorimetry measurements were carried out in an $N_{2(g)}$ atmosphere using a Mettler Toledo STARe DSC3 station instrument equipped with a cryostat. Aluminium capsules were loaded with 30.08 mg of sample, and 60.7 mg of pure sapphire for calibration, and sealed. Heating and cooling rates were fixed at 10 K min^{-1}.

2.2. Synthesis

General procedure for synthesising [Fe(5-F-salEen)$_2$]ClO_4 (1) and [Fe(5-Cl-salEen)$_2$]ClO_4 (2). To start with, 2 mmol of the respective aldehyde was mixed into a solution containing *N*-ethylethylenediamine (210 μL, 2 mmol) in methanol (20 mL). This mixture was stirred for 15 minutes, resulting in a yellow solution. Then, a solution of Fe(II) chloride (127 mg, 1 mmol) and sodium perchlorate (122 mg, 1 mmol) in methanol (10 mL) was filtered into the yellow solution. This addition caused an immediate dark color change due to air oxidation, and the solution was stirred for an additional 30 minutes to yield the [Fe(5-X-salEen)$_2$]ClO_4 complex. Blackish-green, needle-shaped crystals were formed upon solvent evaporation at room temperature under ambient pressure. These crystals were collected by filtration when the solvent volume was reduced to 5 mL and were washed with *n*-hexane and diethyl ether.

[Fe(5-F-salEen)$_2$]ClO_4 (**1**): Used 5-fluorosalicylaldehyde (280 mg, 2 mmol). Yield: 37%. IR (KBr): ν_{max}/cm^{-1} 1629 ($\nu_{C=N}$, s), 1085 (ν_{ClO_4}, s), 625 (ν_{ClO_4}, s). Anal. calculated (%) for $C_{22}H_{28}F_2ClFeN_4O_6$: C, 46.05; H, 4.92; N, 9.76; found: C, 45.75; H, 4.84; N, 9.63%.

[Fe(5-Cl-salEen)$_2$]ClO_4 (**2**): Used 5-chlorosalicylaldehyde (313 mg, 2 mmol). Yield: 31%. IR (KBr): ν_{max}/cm^{-1} 1630 ($\nu_{C=N}$, s), 1091 (ν_{ClO_4}, s), 625 (ν_{ClO_4}, s). Anal. calculated (%) for $C_{22}H_{28}Cl_3FeN_4O_6$: C, 43.55; H, 4.65; N, 9.23; found: C, 43.59; H, 4.53; N, 9.23%.

[Fe(salEen)$_2$]ClO_4 (**3**): This compound was obtained by following a previously reported method.[41] IR (KBr): ν_{max}/cm^{-1} 1630 ($\nu_{C=N}$, s), 1083 (ν_{ClO_4}, s), 625 (ν_{ClO_4}, s). Anal. calculated (%) for $C_{22}H_{30}ClFeN_4O_6$: C, 49.13; H, 5.62; N, 10.42; found: C, 50.01; H, 5.55; N, 10.4.

[Fe(5-Br-salEen)$_2$]ClO_4 (**4**): Polymorphic forms (**4a**, **4b**) were previously reported by us.[35,38] (**4a**) IR (KBr): ν_{max}/cm^{-1} 1630 ($\nu_{C=N}$, s), 1088 (ν_{ClO_4}, s), 1064 (ν_{ClO_4}, s), 624 (ν_{ClO_4}, s). Anal. calculated for $C_{22}H_{28}Br_2ClFeN_4O_6$ (%): C, 37.99; H, 4.06; N, 8.05. Found: C, 37.92; H, 3.82; N, 7.84.

(**4b**) IR (KBr): ν_{max}/cm^{-1} 1633 ($\nu_{C=N}$, s), 1089 (ν_{ClO_4}, s), 1064 (ν_{ClO_4}, s), 625 (ν_{ClO_4}, s). Anal. calculated for $C_{22}H_{28}Br_2ClFeN_4O_6$ (%): C, 37.99; H, 4.06; N, 8.05. Found: C, 37.71; H, 4.06; N, 8.16.

[Fe(5-I-salEen)$_2$]ClO_4 (**5**): This compound has also been previously reported by us.[34] IR (KBr): ν_{max}/cm^{-1} 1632 ($\nu_{C=N}$, s), 1088 (ν_{ClO_4}, s), 625 (ν_{ClO_4}, s). Anal. calculated for

$C_{22}H_{28}I_2ClFeN_4O_6$ (%): C, 33.47; H, 3.57; N, 7.10. Found: C, 33.70; H, 3.65; N, 7.12.

2.3. Crystallography

Crystals suitable for single-crystal X-ray analysis of complexes **1** and **2** were selected and covered with Fomblin (polyfluoro ether oil) and mounted on a nylon loop. Crystallographic data were collected at room temperature and at 110(2) K for complexes **1** and **2** (Table 1) on a Bruker D8 Venture diffractometer equipped with a Photon 100 CMOS detector, and an Oxford Cryosystems Cooler, using graphite monochromated Mo-Kα radiation (λ = 0.71073 Å). The data were processed using the APEX4 suite software package, which includes integration and scaling (SAINT), absorption corrections (SADABS)[42] and space group determination (XPREP). Structure solution and refinement were done using direct methods with the programs SHELXT 2014/5 and SHELXL (version 2018/3)[43] in-built into APEX and WinGX-Version 2021.3[44] software packages. All non-hydrogen atoms were refined anisotropically. Except for NH, all hydrogen atoms were inserted in idealised positions and allowed us to refine riding on the parent carbon atom. The molecular diagrams were drawn with Mercury.[45] The data were deposited with the CCDC under the deposit numbers 2310296 for **1**, 2310297 for **1** (110 K), 2310298 for **2**, and 2310299 for **2** (110 K).†

2.4. Mössbauer studies

Mössbauer measurements were performed at 78 K and at room temperature for **1** and **2** on a conventional constant-acceleration spectrometer equipped with a ^{57}Co(Rh) radioactive source as a 14.4 keV gamma ray provider, a proportional counter that detected the gamma rays passing through the sample, and a multichannel analyzer (CMCA-550), which kept the data counts and transferred data to the computer. To perform a measurement, the source was moved in a triangular waveform with a Doppler velocity of 1.0 mm s^{-1} generated using a Mössbauer drive unit (MR-260A). The sample was kept stationary between the source and the detector. The spectrum was recorded using Wissoft 2003 software and fitted using Recoil software using the Lorentzian site analysis method. The low-temperature measurements were performed using a liquid nitrogen flow cryostat with a temperature stability of ±0.5 K. The spectra were fitted to Lorentzian lines using the WinNormos software program. All isomer shifts (δ) in this work are given with respect to the isomer shift of metallic α-Fe.

2.5. Hirshfeld analysis

The role of intermolecular interactions within the crystal structure was assessed by means of Hirshfeld surfaces.[46,47] Any electron density within the isosurface consists mainly of the contribution of the considered molecules, while that outside the surface is dominated by the remainder of the crystal lattice. The property d_{norm} is composed of two parameters describing the distance of how far away an atom is from the isosurface: d_i if the atom is inside of the surface, and d_e if the atom is outside.[48] It has been mapped on the Hirshfeld surface to give a visual description of the strength of the contacts across the whole molecule using a colour scale. Strengthened intermolecular interactions that have short contacts are represented

Table 1 Crystallographic data and refinement details of structures **1** and **2** at room temperature and at 110 K

	1	**1**-110 K	**2**	**2**-110 K
Formula	$C_{22}H_{28}ClF_2FeN_4O_6$	$C_{22}H_{28}ClF_2FeN_4O_6$	$C_{22}H_{28}Cl_3FeN_4O_6$	$C_{22}H_{28}Cl_3FeN_4O_6$
M	573.78	573.78	606.68	606.68
λ (Å)	0.71073	0.71073	0.71073	0.71073
T (K)	300(2)	110(2)	300(2)	110(2)
Crystal system	Monoclinic	Monoclinic	Monoclinic	Monoclinic
Space group	$P2_1/c$	$P2_1/c$	$P2_1/c$	$P2_1/c$
Crystal description	Block	Block	Block	Prism
Crystal color	Brown	Brown	Black	Black
a (Å)	10.123(2)	9.8076(5)	9.9911(10)	9.8405(5)
b (Å)	21.819(5)	21.5134(10)	23.030(2)	22.8166(9)
c (Å)	12.084(3)	12.1084(6)	12.0882(11)	11.9228(6)
α (°)	90	90	90	90
β (°)	103.742(12)	104.487(2)	103.748(4)	104.146(2)
γ (°)	90	90	90	90
V (Å^3)	2592.8(11)	2473.6(2)	2701.8(5)	2595.8(2)
Z	4	4	4	4
ρ_{calc} (g cm^{-3})	1.470	1.541	1.491	1.552
μ (mm^{-1})	0.743	0.779	0.898	0.935
θ_{max} (°)	25.146	25.072	28.290	25.701
Total data	30 503	36 275	136 496	53 569
Unique data	4595	4389	6714	4923
R_{int}	0.1281	0.0799	0.2596	0.1102
R [$I > 3\sigma(I)$]	0.0580	0.0391	0.0623	0.0359
wR_2	0.1364	0.0907	0.1458	0.0687
Goodness of fit	1.016	1.054	1.026	1.027
ρ_{min}	−0.403	−0.457	−0.624	−0.476
ρ_{max}	0.459	0.607	0.190	0.306

as extremely red areas of colour on the Hirshfeld surface, which means regions where the value of d_{norm} is negative and the sum of d_i and d_e is less than the sum of the van der Waals radii. On the other hand, the weakest interactions with long contacts have the blue colour passing through white for intermediate interactions. The CrystalExplorer software[49] has been used in the calculation of the Hirshfeld surfaces in the crystal lattice, giving information on the crystal packing and the strength of the intermolecular interactions within the lattice. All the points on the Hirshfeld surface were also represented in the form of 2D fingerprint plots.[50] The fingerprint plots provide a correlation between d_e and d_i, which corresponds to the distance to the nearest external and internal atoms, respectively. The colour of the 2D graph also indicates the density of the points in the region. The red colour indicates a high number of interactions corresponding to that of the [d_e, d_i] region and when the density of the points decreases, the colour changes to blue passing through green. The fingerprint plots give information about the type, the density and the strength of the interactions.

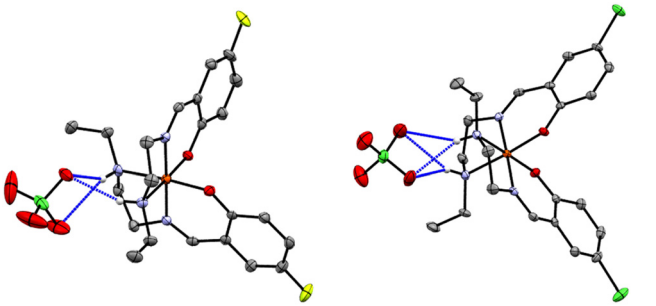

Fig. 1 ORTEP views of compounds (a) **1** and (b) **2**, at 110 K, represented with 50% probability level ellipsoids. All hydrogen atoms, with the exception of those involved in hydrogen bonding with the perchlorate counterion, are omitted for clarity. Atom colours: carbon: grey, hydrogen: white, nitrogen: blue, oxygen: red, chlorine: green, fluorine: yellow, and iron: orange. N–H···O hydrogen bonds are represented by blue dashed lines.

3. Results

3.1. Chemical studies

Two Fe(III) complexes with perchlorate as the anion were synthesised using a reaction that involved the condensation of *N*-ethylethylenediamine (Een) with either 5-fluorosalicylalde-hyde or 5-chlorosalicylaldehyde, metalation with Fe(II) chlor-ide, and anion metathesis with sodium perchlorate. Fe(III) crys-talline complexes (**1** and **2**, Scheme 1) were obtained after air oxidation and slow evaporation of the solvent. It should be noted that although the final complexes are Fe(III), the syn-thesis of the complexes strategically began with Fe(II) to increase the likelihood of obtaining unsolvated complexes. The complexes were characterised in the solid state by elemen-tal analysis, IR spectroscopy, single-crystal X-ray diffraction, ^{57}Fe Mössbauer spectroscopy, SQUID magnetometry and differential scanning calorimetry (DSC). The formation of the imine bond in the ligand was confirmed by the presence of a C=N stretching band in the IR spectra of these complexes at 1629 cm^{-1} (**1**) and 1630 cm^{-1} (**2**), as shown in Fig. S1.† Successful anion exchange upon formation of the complexes was confirmed by the presence of stretching bands assigned to the ClO_4^- anions at 1085 and 625 cm^{-1} (**1**) and 1091 and 625 cm^{-1} (**2**) (Fig. S1†). The purity of the compounds was confirmed through elemental analysis.

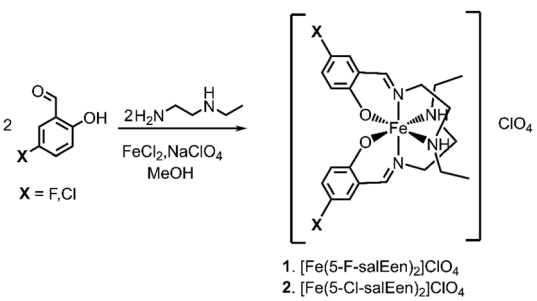

Scheme 1 Synthesis of Fe(III) complexes **1** and **2**.

3.2. Structural characterisation of 1 and 2

Compounds **1** and **2** are isomorphous and crystallised in the monoclinic space group $P2_1/c$, and their molecular structures established at 110 K are depicted in Fig. 1, while those determined at 300 K can be found in Fig. S2 (**1**) and S3 (**2**), in the ESI.†

The asymmetric unit of both complexes comprises one cation and one anion. In both cases the anion is hydrogen bonded to the cation *via* the hydrogen of the nitrogen amines of the ligand at both temperatures with no significant differences in N–H···O bond lengths or the Fe–Cl_{anion} distance either at low or high temperature. The ligand coordinates in a meridional fashion and the bond lengths around the metal centre are depicted in Table 2.

The bond lengths for **1** and **2** at 110 K are typical of Fe(III) LS and at 300 K represent very well the compounds predominantly in the HS state. This indicates that both compounds undergo spin state changes and the shape of the curve will be determined by magnetic studies. The geometry around the

Table 2 Bond lengths of the Fe(III) coordination sphere at 110 and 300 K for **1** and **2**

Compound	Bond	Distance (Å)			
		110 K		300 K	
1	Fe–N_{im}	1.928(2)	1.927(2)	2.057(3)	2.056(3)
	Fe–N_{am}	2.045(2)	2.042(2)	2.173(3)	2.184(4)
	Fe–O	1.870(2)	1.868(2)	1.893(3)	1.901(3)
2	Fe–N_{im}	1.929(2)	1.937(2)	2.094(3)	2.102(2)
	Fe–N_{am}	2.042(2)	2.053(2)	2.225(2)	2.209(2)
	Fe–O	1.863(2)	1.877(2)	1.913(2)	1.905(2)

metal centre is slightly distorted octahedral, with small deviations from the expected 180° and 90° observed for a pure octahedron (Table S1†). Although the differences are very small, these distortions are more evident at 300 K than at 110 K. The intermolecular interactions present in both compounds and at both temperatures were analysed. Complexes **1** and **2**, due to their isostructurality, show similar crystal packing, when viewed along the *c* axis, at both temperatures (Fig. S4(a)–(d)†). Nevertheless, these supramolecular arrangements are obtained through the establishment of different intermolecular interactions, depicted in Fig. S5–S8.† These include classical and non-classical hydrogen bonds [N–H···O and C–H···O, respectively], halogen bonds [C–H···X (X = F, Cl), Cl···π and Cl···Cl], and π···π and C–H···π. The main difference between the observed interactions in **1** and **2** is that in **1**, it is possible to observe π···π stacking between two antiparallel 5-F-aryl rings, whereas in **2**, only C–H···π, π···Cl and Cl···Cl are present.

Both compounds were obtained in the form of needle-shaped crystals and to confirm the sample purity, powder X-ray diffraction measurements were done. The powder X-ray diffraction patterns experimentally obtained for both compounds agree with the simulated diffraction patterns calculated through the SCRX data, indicating that the compounds are pure (Fig. S9†).

3.3. Hirshfeld analysis of 1 and 2

The Hirshfeld surface plots obtained with the Crystal Explorer software[49] for **1** and **2** both in the LS and HS states are shown in Fig. 2.

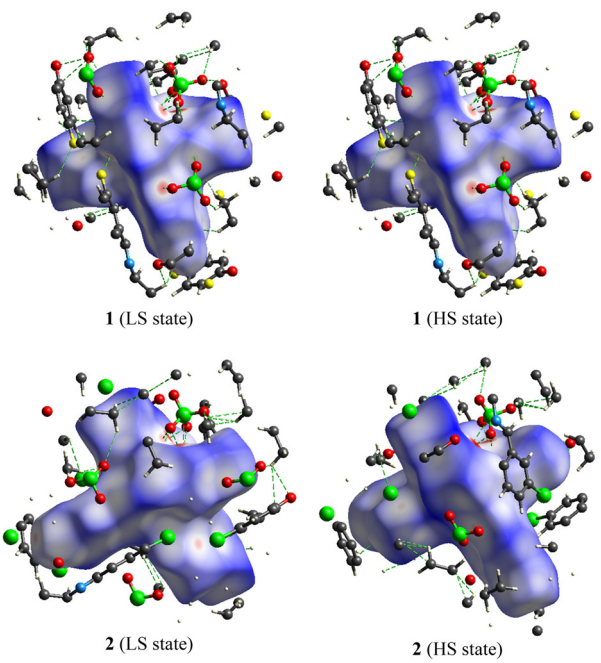

Fig. 2 Hirshfeld surfaces within the crystal lattice for **1** and **2** excluding the ClO_4^- counterion from the surface. For these compounds, the most strengthened intermolecular interactions are shown in red, which correspond to H···O, H···π, H···X and H···H interactions.

The Hirshfeld surfaces demonstrate the role of the intermolecular interactions in providing a network of intermolecular contacts between the cation and its ClO_4^- anion or other neighbouring cations within the crystal lattice both in the HS and LS states. Such intermolecular interactions are present due to different functional groups depending on the functionalisation of the metal complex (N–H, C–H, aromatic rings, halogens, *etc.*). The Hirshfeld surface of the F- and Cl-derived cations displays red regions of the isosurface in both spin states, which represent hydrogen bonding at the H···O, H···π, H···X and H···H sites between the cation and its ClO_4^- counterion or other neighbouring cations. The ClO_4^- anions place themselves in the lattice to produce the C–H···O and N–H···O intermolecular interactions. Non-conventional H···H intermolecular hydrogen bonding interactions are also present and have already been described in previous works.[51–55]

On the other hand, Fig. S10–S13† show the 2D fingerprints derived from Hirshfeld surfaces of complexes **1** and **2** for the intermolecular interactions H···π, H···X, H···H and H···O, respectively.

It is observed from the Hirshfeld surface of **1** and **2** that the most important intermolecular interactions are H···π (H···C), H···X, H···H and H···O. The interaction of C–H and especially N–H groups with ClO_4^- molecules are the most strengthened interactions, which was indicated by the darker red colour on the Hirshfeld surfaces (see Fig. 2). On the other hand, the H···H interactions between cations within the lattice would be the weakest interaction once the red colour was lighter on the Hirshfeld surfaces. H···π interactions would be in the middle and in the case of H···X interactions, it depends on the halogen atom, where the interactions with the most electronegative F atom have the darkest red colour on the Hirshfeld surfaces. These findings are also observed on the fingerprint plot, in which the N–H···O area of the interaction of cations of **1** and **2** with the ClO_4^- anion reaches shorter (d_e, d_i) values (around 1.2 and 0.8, respectively). The other intermolecular interactions between the cations of **1** and **2** within the lattice are weaker and include especially H···π, H···X, H···H and other H···O interactions, in particular C–H···O interactions.

3.4. Magnetic properties

The magnetic profiles of both compounds were obtained in the temperature range 10–370 K and the data were acquired every 5 K, as shown in Fig. 3.

The $\chi_M T$ value of **1** at 370 K is 4.5 cm^3 mol^{-1} K, which corresponds to HS Fe(III). While cooling, the population of spin states changes very gradually down to 250 K and then more rapidly between 250 and 125 K, showing an inflection point at around 165 K. At 125 K there is a sharp change in $\chi_M T$ down to 100 K, and from there down the spin population changes again gradually. At 10 K the $\chi_M T$ value of **1** is 1.1 cm^3 mol^{-1} K, which corresponds to 15% HS. The compound follows the same path while warming up; however, at around 110 K, a negligible hysteresis window opens up with a width of 1 K. The $\chi_M T$ value of **2** at 370 K is 4.3 cm^3 mol^{-1} K, which corresponds to HS Fe(III). The magnetic profile of this compound is typical of a HS/LS switch where the compound

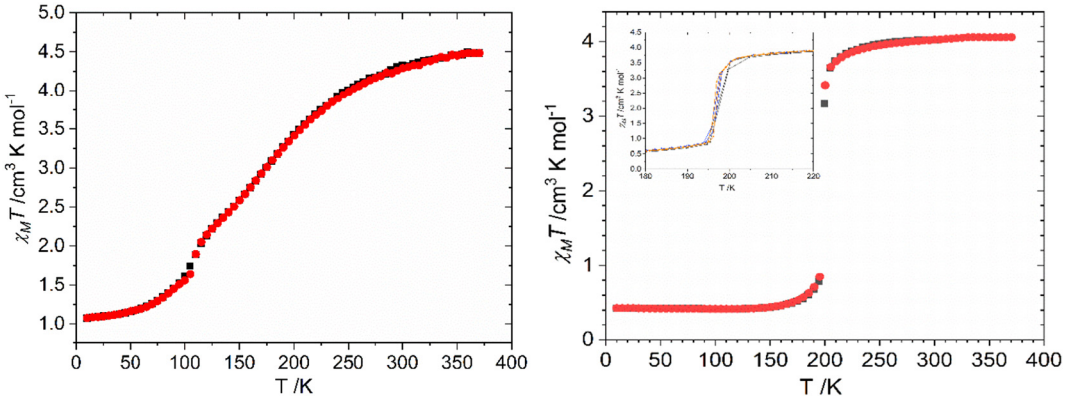

Fig. 3 $\chi_M T$ *vs.* T values of **1** (left) and **2** (right).

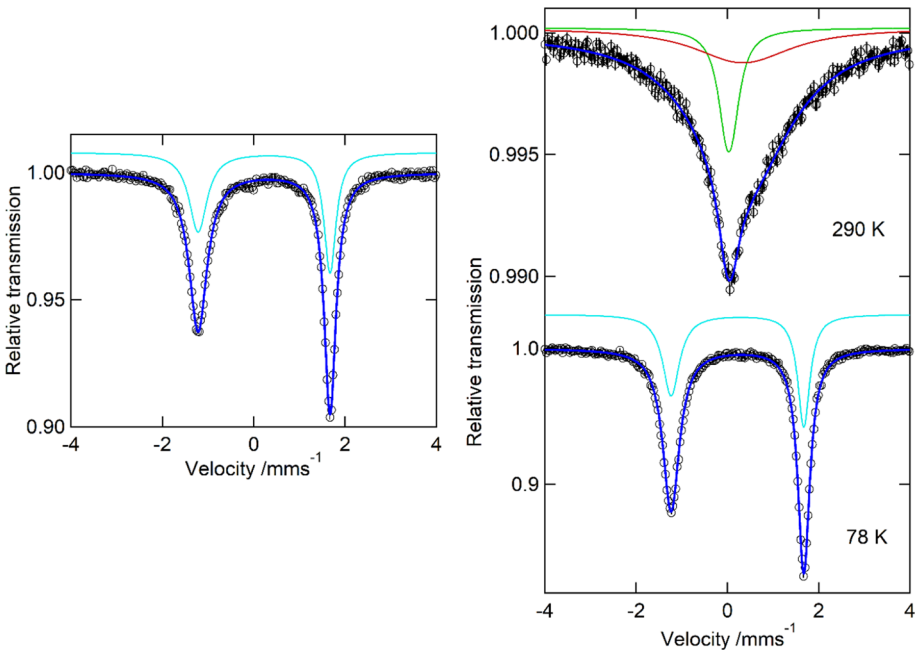

Fig. 4 Mössbauer spectra of compound **1** (left) at 78 K and compound **2** (right) at 78 and 290 K.

adopts the HS state down to 200 K, below which it transitions to the low-spin state over a range of 10 K, resulting in a $T_{1/2}$ = 194 K. From 190 K down to 10 K, the compound is in the LS state, with a $\chi_M T$ value of 0.44 cm^3 mol^{-1} K at 10 K. Scan rate-dependent studies (5, 2 and 1 K min^{-1}) reveal a 1 K hysteresis loop and $T_{1/2}$ = 196 K, as shown in Fig. 3 (inset).

Table 3 Isomer shifts, quadrupole splitting and line half widths of **1** at 78 K and **2** at 78 and 290 K

Compound	T (K)		δ (mm s^{-1})	ΔE_Q (mm s^{-1})	Γ (mm s^{-1})	%
1	78		0.225(2)	2.887(3)	0.480(4)	100
2	78		0.219(6)	2.907(1)	0.444(2)	100
	290	Red	0.34(2)	0.4(3)	2.4(2)	88.4
		Green	0.03(1)	0.13(8)	0.45(9)	11.6

^{57}Fe Mössbauer spectra, both at 78 and 290 K, were also used to understand the magnetic behaviour of bulk samples of **1** and **2**, as revealed in Fig. 4. The isomer shift, quadrupole splitting, and line half widths are given in Table 3.

The Mössbauer spectrum of **1** at 78 K displays a single quadrupole doublet well fitted with typical Fe(III) hyperfine parameters with δ_{LS} = 0.225(2) mm s^{-1} and large quadrupole splitting $\Delta E_{Q_{LS}}$ = 2.887(3) mm s^{-1}, characteristic of the LS state, which fit well with crystallographic and SQUID data. The Mössbauer spectrum of **2** at 78 K also displays a single quadrupole doublet well fitted with typical Fe(III) hyperfine parameters with δ_{LS} = 0.219(6) mm s^{-1} and an even larger quadrupole splitting $\Delta E_{Q_{LS}}$ = 2.907(1) mm s^{-1}, characteristic of the LS state, once again fitting well with crystallographic and SQUID data. The Mössbauer spectrum of **2** recorded at room temperature clearly shows two quadrupole doublets, indicating a poss-

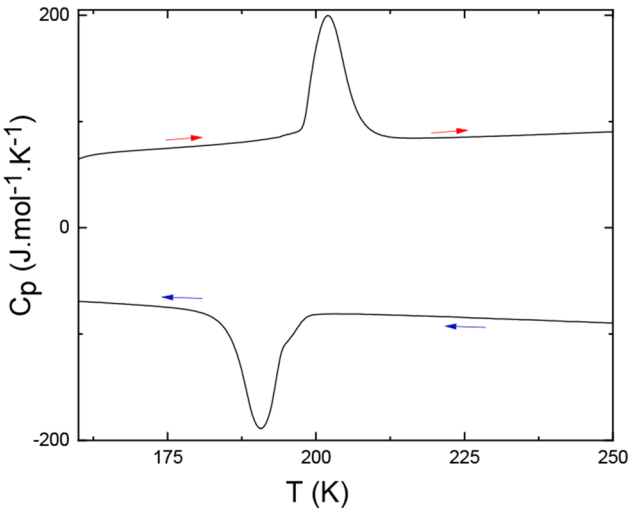

Fig. 5 Heat capacity profile during the cooling and warming modes of compound **2**.

ible spin state mixture, in agreement with SQUID measurements. The spectrum was fitted with two quadrupole doublets with isomer shifts δ = 0.34(2) mm s^{-1} and δ = 0.03(1) mm s^{-1} characteristic of Fe(III) ions. Analysis of quadrupole splitting values yielded $\Delta E_{Q_{LS}}$ = 0.13(8) mm s^{-1}, which is characteristic of LS ions with a valence contribution to the electric field gradient, which is cancelled in the HS state, as shown by $\Delta E_{Q_{HS}}$ = 0.4(3) mm s^{-1}. The HS/LS mixture of spin states was evaluated as 88.4%/11.6%. At the same temperature, SQUID results indicated a nearly full conversion of Fe(III) to the HS state.

3.5 Differential scanning calorimetry (DSC)

DSC measurements (Fig. 5) were recorded for compound **2** over the range 153–298 K in cooling and warming modes, at 10 K min^{-1}, given the temperature range of the SCO by SQUID magnetometry (Fig. 3).

Upon cooling, an exothermic peak is clearly identified below 200 K at an onset temperature $T_0^{\downarrow}$ = 195 K. On warming up back to room temperature, an endothermic peak develops above 190 K with $T_0^{\uparrow}$ = 197 K. These peaks are the signature of a first-order phase transition, with transition temperatures in agreement with SQUID magnetometry. The enthalpy and entropy data were evaluated as ΔH = 5.97 kJ mol^{-1} and ΔS = 30.46 J mol^{-1} K^{-1}, respectively, considering a transition of 88.4% of iron sites, according to Mössbauer spectroscopy (Table 3). The latter value is much higher than the electronic value $\Delta S_e = R\ln(6/2)$ = 9.13 J mol^{-1} K^{-1}, which could indicate a vibrational contribution to the entropy data, ΔS_{vib} = 21.33 J mol^{-1} K^{-1}, in the absence of a structural transition associated with the SCO behaviour.

4. Discussion

The $T_{1/2}$ values of compounds **1**–**5** are presented in Table S2†. The magnetic profiles of compounds **1** and **2** are discussed in section 3. For compound **3**, the $\chi_M T$ values start at 3.92 cm^3 mol^{-1} K at 350 K, gradually decreasing to a constant 0.45 cm^3 mol^{-1} K below 125 K. This gradual decrease suggests the transition from an HS to an LS state, with a transition temperature ($T_{1/2}$) of 215 K.[41] Compound **4a** displays a more defined transition, with $\chi_M T$ values showing a sharp change in the range of 165–175 K and a $T_{1/2}$ value of 172 K, coupled with a minor hysteresis of 1 K, indicating a nearly complete SCO with reproducible cooling and heating cycles.[35] The magnetic profile of **4b** is characterised by a large hysteresis window at room temperature and a complex transition involving multiple processes, indicating cooperative behaviour.[38] Finally, compound **5** exhibits an incomplete spin transition centred close to room temperature, with a narrow hysteresis loop observed only in the initial cycle, leading to stabilisation in subsequent cycles, similar to the behaviour observed in **4b**, albeit with differences in the hysteresis loop size and transition completeness.[34]

To evaluate the impact of aromatic ring functionalisation on the magnetic properties of non-solvated X-salEen (X = H, F, Cl, Br, and I) ligand Fe(III) perchlorate complexes, Hirshfeld analysis (Fig. S10–S17†) was employed alongside the octahedral distortion assessment using OctaDist software (Table 4).[56] The new compounds (**1** and **2**) were compared against the previously reported [Fe(salEen)$_2$]ClO$_4$ (**3**), the two polymorphic forms of [Fe(5-Br-salEen)$_2$]ClO$_4$ (**4a**, **4b**) and [Fe(5-I-salEen)$_2$]ClO$_4$ (**5**).

In the computational assessment using the OctaDist software, a systematic evaluation of distortion parameters was undertaken. For all analysed cases, there is a consistent trend of the average bond length elongation around the metal centre as a function of temperature. Distortion deviations from the ideal octahedral geometry can be quantified using Σ values. Notably, while the octahedral distortion intensifies in the majority of cases, the trend for compound **4b** is the opposite. This anomalous behaviour is unanticipated. Such a trend can be potentially correlated with the structural phase transition and thermosalient effect detected at temperatures above room temperature.[38] The geometric deviation from a pristine octahedral (O_h) configuration to a trigonal prismatic (D_{3h}) form is characterised by Θ. It is evident that compounds exhibiting pronounced deviations from the perfect octahedral geometry

Table 4 $\langle D\rangle$, Σ and Θ of compounds **1**–**5**

Compound	T (K)	$\langle D\rangle$ (Å)	Σ (°)	Θ (°)
1	110	1.947	45.08	127.41
	300	2.044	54.36	200.05
2	110	1.950	41.61	121.28
	300	2.074	63.96	237.96
3	100	1.954	46.21	132.21
	300	2.051	57.90	201.38
4a	105	1.953	38.09	116.20
	300	2.074	62.74	240.56
4b	125	1.946	52.73	153.43
	300	1.991	40.06	134.92
5	110	1.952	37.42	104.85
	350	2.013	47.02	168.48

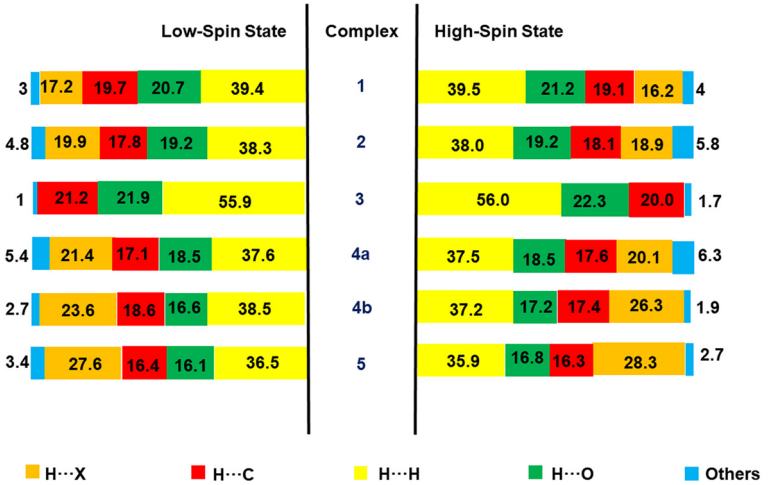

Fig. 6 Hirshfeld surface analysis results depicting the considered weak interactions present in the studied complexes (**1**, **2**, **3**, **4a**, **4b** and **5**).

(*e.g.*, **2**, **4a**) manifest abrupt transitions and, subsequently, a higher HS state population. Intriguingly, and in agreement with the aforementioned observation for the Σ value, compound **4b** exhibits a trend reversal compared to its counterparts. The graphical representation of Θ against $\langle D \rangle$ elucidates the correlation between distortion parameters and magnetic profiles, as depicted in Fig. S18.† Compounds that exhibit abrupt SCO, namely **2** and **4a**, manifest similar correlation trends among themselves based on the values obtained. Conversely, compounds that show gradual SCO display characteristics distinct from the aforementioned compounds; yet, they exhibit mutual relationships. It is noteworthy that the difference between the values at low and high temperatures is smaller for compounds **1** and **3** compared to **2** and **4a**. Compounds **4b** and **5**, characterised by their unique profiles, lack mutual correlation and do not follow a linear trend.

To gain deeper insights into the behaviour and trends of the compounds, we focused on understanding how the SCO phenomenon is influenced by interactions such as H···π, H···O, H···X, and H···H across all compounds. Our attention was directed towards assessing how these interactions impact the transition between spin states in complexes featuring halogen-substituted aromatic rings compared to their non-substituted counterparts. Through our analysis, we identified patterns and variations that underscored the role and adjustability of these interactions based on different halogen substitutions and structural configurations, as shown in Fig. 6.

In the case of the non-substituted complex **3**, the LS state predominantly exhibits contributions to H···π interactions, while the HS state marginally demonstrates higher contributions to H···O interactions. Notably, there are no significant differential contributions observed for H···H interactions between the LS and HS states. Similar behaviour is observed for the compound containing F in the aromatic ring (**1**), where the H···H interactions exhibit comparable behaviour.

Furthermore, the HS state shows slightly increased contributions to H···O interactions, while the LS state displays more pronounced contributions to H···π interactions. Regarding H···X interactions, the LS state yields the most significant contribution.

For the compound containing Cl in the aromatic ring (**2**), it is evident that the LS state offers the most substantial contribution to the H···X interactions, with no discernible differences noted for other interactions between the LS and HS states. The compound containing Br in the aromatic ring (**4**) presents two polymorphic structures (**4a**, **4b**), with distinct behaviours. In **4b**, where a pure HS state is never attained, and a mixture of HS/LS is obtained at high temperatures, conclusions regarding the HS contribution must be approached cautiously.

Regarding intermolecular weak interactions and the magnetic plot related to LS to HS transitions, significant differences are observed between compounds **1**, **2**, and the rest (**3**, **4a**, **4b**, **5**). For compounds with abrupt transitions, such as **2** and **4a**, contributions from O···H interactions remain constant across both spin states. Conversely, for more gradual transitions, the O···H contribution is predominantly more important in the HS state.

Compounds **5** and **4b** exhibit a mixture of spin states as the temperature increases, differing from the other compounds. Specifically, the contributions of H···X interactions for these compounds are more important at higher temperatures. Additionally, H···H interactions are more significant for the LS state in **5** and **4b**.

Considering H···X interactions, their importance follows the order: I > Br > Cl > F. Notably, while H···H contributions predominate, they are inherently weaker compared to other interactions. Furthermore, the strength of the H···X interaction inversely aligns as F > Cl > Br > I. The significance of the H···X interaction in each compound affects the cooperative effect between molecules in the crystal system, leading to changes in magnetic profiles.

5. Conclusions

We performed a comparative analysis of the different halogen-substituted ligands F (**1**), Cl (**2**), H (**3**), Br (**4a**, **4b**) and I (**5**) and tried to extract trends. While **1** shows a gradual transition in several steps with a small hysteresis loop around 100 K, **2** shows a complete and abrupt transition at around 200 K with $T_{1/2}$ = 195 K. Compound **3** shows a gradual and complete SCO with $T_{1/2}$ = 230 K. The profile of **2** is very similar to the profile of **4a**, however, the latter with $T_{1/2}$ = 172 K. Compounds **4b** and **5** show very similar magnetic profiles with **4b** retaining the hysteresis window and asymmetric profile around room temperature and **5** displaying only one initial hysteretic profile followed by a gradual transition after the first cycle. In our comprehensive analysis aimed at discerning the effects of aromatic ring functionalization on the magnetic properties of non-solvated X-salEen-ligand Fe(III) perchlorate complexes, we used Hirshfeld analysis and OctaDist software for the octahedral distortion assessment. A comparative study was conducted between newly synthesized compounds (**1** and **2**) and previously reported complexes (**3**, **4a**, **4b**, and **5**). Our analysis revealed a uniform trend of average bond length elongation around the metal center, influenced by temperature. Deviations from the ideal octahedral geometry were quantified using Σ values. Notably, compound **4b** displayed a different trend from its counterparts, suggesting possible connections to structural phase transitions and thermosalient effects at high temperatures. Examining the SCO phenomenon, we observed patterns reflecting the influence of intermolecular interactions, specifically H···π, H···O, H···X, and H···H, on the LS to HS transition in halogen-substituted aromatic ring complexes. Our data showcased distinct interaction contributions for each complex and highlighted the nuanced roles these interactions play in magnetic transitions. For compounds exhibiting abrupt SCO transitions, the data indicated exactly the same value for the relative contribution of the atom pairs from O···H intermolecular interactions between the cation and the ClO_4^- anion in both spin states: LS and HS (19.2% in the case of **2** and 18.5% in the case of **4a**). However, for compounds showcasing more gradual transitions, the O···H contribution favored the HS state. In addition, for the most abrupt SCO transitions, the values for relative contributions in H···C of the H···π interactions are higher for the HS state than for the LS state. This trend is the opposite in the case of gradual transitions, in which the values for relative contributions in H···C of the H···π interactions are higher for the LS state and lower for the HS state. Nevertheless, the strength of the H···X interaction is inversely correlated as F > Cl > Br > I. Finally, while H···H contributions were dominant, they inherently exhibited weaker interactions compared to H···π, H···O, and H···X. Our work highlights the intricate interplay of halogen substitution, aromatic ring functionalization, and intermolecular interactions in influencing magnetic properties. These findings underscore the tunability of these interactions and provide key insights into the design and understanding of similar molecular systems.

Conflicts of interest

There are no conflits to declare.

Acknowledgements

Centro de Química Estrutural (CQE) and the Institute of Molecular Sciences (IMS) acknowledge financial support from Fundação para a Ciência e Tecnologia (Projects UIDB/00100/2020 (https://doi.org/10.54499/UIDB/00100/2020), UIDP/00100/2020 (https://doi.org/10.54499/UIDP/00100/2020), and LA/P/0056/2020 (https://doi.org/10.54499/LA/P/0056/2020), respectively). BioISI acknowledges FCT for financial support (UIDB/04046/2020 and UIDP/04046/2020). Centro de Física Teórica e Computacional (CFTC) acknowledges FCT under Contract nos. UIDB/00618/2020 (**https://doi.org/10.54499/UIDB/00618/2020**) and UIDP/00618/2020 (**https://doi.org/10.54499/UIDP/00618/2020**). This work was supported by the FNRS (PDR T.0095.21, CDR J.0064.23, EQP U.N027.24). Clara S. B. Gomes acknowledges the Associate Laboratory for Green Chemistry – LAQV, which is financed by national funds from Fundação para a Ciência e a Tecnologia (UIDB/50006/2020 (https://doi.org/10.54499/UIDB/50006/2020), UIDP/50006/2020 (https://doi.org/10.54499/UIDP/50006/2020) and LA/P/0008/2020 (https://doi.org/10.54499/LA/P/0008/2020)) and the XTAL – Macromolecular Crystallography group (UCIBIO and i4HB) for granting access to the X-ray diffractometer. The X-ray infrastructure was financed by FCT-MCTES through project RECI/BBBBEP/0124/2012. Sónia Barroso thanks Project SmartBioR for financial support (CENTRO-01-0145-FEDER-000018). Sónia Barroso is also grateful to Centro de Química Estrutural for access to its crystallography facilities. Marcos A. Bento thanks FCT for the PhD scholarship (2021.07918.BD). Paulo N. Martinho thanks FCT and RSC for financial support (grants PTDCQUI-QIN0252_2021 (https://doi.org/10.54499/PTDC/QUI-QIN/0252/2021) and R21-7511142525). Paulo N. Martinho also thanks FCT for the contract CEECIND/00509/2017 (https://doi.org/10.54499/CEECIND/00509/2017/CP1387/CT0029). Adrià Gil is a Serra Húnter Fellow and is very grateful to the Serra Húnter Programme for allowing him to proceed with his research studies. COST Actions CA21101 (COSY) and CA22131 (LUCES) are also acknowledged.

References

1 M. G. Reeves, E. Tailleur, P. A. Wood, M. Marchivie, G. Chastanet, P. Guionneau and S. Parsons, Mapping the cooperativity pathways in spin crossover complexes, *Chem. Sci.*, 2021, **12**, 1007–1015.

2 P. Gütlich and H. A. Goodwin, Spin Crossover - An Overall Perspective, *Top. Curr. Chem.*, 2004, **233**, 1–47.

3 A. Hauser, Ligand Field Theoretical Considerations, *Top. Curr. Chem.*, 2004, **233**, 49–58.

4 P. Gütlich, A. B. Gaspar and Y. Garcia, Spin state switching in iron coordination compounds, *Beilstein J. Org. Chem.*, 2013, **9**, 342–391.

5 M. A. Halcrow, Spin-crossover Compounds with Wide Thermal Hysteresis, *Chem. Lett.*, 2014, **43**, 1178–1188.

6 G. Molnár, M. Mikolasek, K. Ridier, A. Fahs, W. Nicolazzi and A. Bousseksou, Molecular Spin Crossover Materials: Review of the Lattice Dynamical Properties, *Ann. Phys.*, 2019, **531**, 1900076.

7 T. K. Ekanayaka, K. P. Maity, B. Doudin and P. A. Dowben, Dynamics of Spin Crossover Molecular Complexes, *Nanomaterials*, 2022, **12**, 1742.

8 S. Zheng, M. A. Siegler, O. Roubeau and S. Bonnet, Influence of Selenocyanate Ligands on the Transition Temperature and Cooperativity of bapbpy-Based Fe(II) Spin-Crossover Compounds, *Inorg. Chem.*, 2014, **53**, 13162–13173.

9 I. Nemec, R. Herchel, R. Herchel, R. Boča, Z. Trávníček, I. Svoboda, H. Fuess and W. Linert, Tuning of spin crossover behaviour in iron(III) complexes involving pentadentate Schiff bases and pseudohalides, *Dalton Trans.*, 2011, **40**, 10090–10099.

10 S. Zheng, N. R. M. Reintjens, M. A. Siegler, O. Roubeau, E. Bouwman, A. Rudavskyi, R. W. A. Havenith and S. Bonnet, Stabilization of the Low-Spin State in a Mononuclear Iron(II) Complex and High-Temperature Cooperative Spin Crossover Mediated by Hydrogen Bonding, *Chem. – Eur. J.*, 2016, **22**, 331–339.

11 F. X. Shen, Q. Pi, L. Shi, D. Shao, H. Q. Li, Y. C. Sun and X. Y. Wang, Spin crossover in hydrogen-bonded frameworks of FeII complexes with organodisulfonate anions, *Dalton Trans.*, 2019, **48**, 8815–8825.

12 S. Hayami, K. Hiki, T. Kawahara, Y. Maeda, D. Urakami, K. Inoue, M. Ohama, S. Kawata and O. Sato, Photo-Induced Spin Transition of Iron(III) Compounds with π–π Intermolecular Interactions, *Chem. – Eur. J.*, 2009, **15**, 3497–3508.

13 B. J. C. Vieira, J. C. Dias, I. C. Santos, L. C. J. Pereira, V. Da Gama and J. C. Waerenborgh, Thermal Hysteresis in a Spin-Crossover FeIII Quinolylsalicylaldimine Complex, FeIII(5-Br-qsal)$_2$Ni(dmit)$_2$·solv: Solvent Effects, *Inorg. Chem.*, 2015, **54**, 1354–1362.

14 V. M. Hiiuk, S. Shova, A. Rotaru, A. A. Golub, I. O. Fritsky and I. A. Gural'Skiy, Spin crossover in 2D iron(II) phthalazine cyanometallic complexes, *Dalton Trans.*, 2020, **49**, 5302–5311.

15 R. Díaz-Torres, G. Chastanet, E. Collet, E. Trzop, P. Harding and D. J. Harding, Bidirectional photoswitchability in an iron(III) spin crossover complex: symmetry-breaking and solvent effects, *Chem. Sci.*, 2023, **14**, 7185–7191.

16 R. Busch, A. B. Carter, K. F. Konidaris, I. A. Kühne, R. González, C. E. Anson and A. K. Powell, The First Use of a ReX_5 Synthon to Modulate FeIII Spin Crossover via Supramolecular Halogen···Halogen Interactions, *Chem. – Eur. J.*, 2020, **26**, 11835–11840.

17 F. Kobayashi, K. Iwaya, H. Zenno, M. Nakamura, F. Li and S. Hayami, Spin State Modulation in Cobalt(II) Terpyridine Complexes by Co-crystallization with 1,3,5-Triiodo-2,4,6-trifluorobenzene, *Bull. Chem. Soc. Jpn.*, 2021, **94**, 158–163.

18 H. Zenno, R. Akiyoshi, M. Nakamura, Y. Sekine and S. Hayami, Crystal Structures and Spin Crossover of Iron(III) Cocrystal Formed via Halogen Bonding, *Chem. Lett.*, 2021, **50**, 1259–1262.

19 Y. Avila, R. Mojica, M. C. Vázquez, L. Sánchez, M. González, J. Rodríguez-Hernández and E. Reguera, Spin-crossover in the Fe(4X-pyridine)$_2$[Fe(CN)$_5$NO] series with X = Cl, Br, and I. Role of the distortion for the iron atom coordination environment, *New J. Chem.*, 2022, **47**, 238–249.

20 N. Suryadevara, A. Mizuno, L. Spieker, S. Salamon, S. Sleziona, A. Maas, E. Pollmann, B. Heinrich, M. Schleberger, H. Wende, S. K. Kuppusamy and M. Ruben, Structural Insights into Hysteretic Spin–Crossover in a Set of Iron(II)-2,6-bis(1*H*-Pyrazol-1-yl) Pyridine) Complexes, *Chem. – Eur. J.*, 2022, **28**, e202103853.

21 O. Y. Horniichuk, K. Ridier, G. Molnár, V. O. Kotsyubynsky, S. Shova, V. M. Amirkhanov, I. A. Gural'skiy, L. Salmon and A. Bousseksou, Solvatomorphism, polymorphism and spin crossover in bis[hydrotris(1,2,3-triazol-1-yl)borate]iron(II), *New J. Chem.*, 2022, **46**, 11734–11740.

22 B. Dey, J. Cirera, S. Mehta, L. P. Ferreira, R. Arumugam, A. Mondal, P. N. Martinho and V. Chandrasekhar, Steric Effects on Spin States in a Series of Fe(III) Complexes, *Cryst. Growth Des.*, 2023, **23**, 6668–6678.

23 J. Herz, R. Meyer, J. A. Wolny, V. Schünemann and H. M. Urbassek, Crystal effects in the vibrational spectra of one-dimensional molecular spin crossover crystals using molecular dynamics simulations, *Appl. Phys. A*, 2023, **129**, 345.

24 M. A. Halcrow, *Spin-Crossover Materials: Properties and Applications*, John Wiley & Sons Ltd, Oxford, UK, 2013.

25 M. Halcrow, B. Weber, M. Yamashita and S. Konar, Molecular Magnets and Switchable Magnetic Materials, *Cryst. Growth Des.*, 2023, **23**, 6219–6220.

26 P. N. Martinho, F. F. Martins, N. A. G. Bandeira and M. J. Calhorda, Spin Crossover in 3d Metal Centers Binding Halide-Containing Ligands: Magnetism, Structure and Computational Studies, *Sustainability*, 2020, **12**, 2512.

27 K. Pandurangan, B. Gildea, C. Murray, C. J. Harding, H. Müller-Bunz and G. G. Morgan, Lattice Effects on the Spin-Crossover Profile of a Mononuclear Manganese(III) Cation, *Chem. – Eur. J.*, 2012, **18**, 2021–2029.

28 B. Gildea, L. C. Gavin, C. A. Murray, H. Müller-Bunz, C. J. Harding and G. G. Morgan, Supramolecular modulation of spin crossover profile in manganese(III), *Supramol. Chem.*, 2012, **24**, 641–653.

29 B. Gildea, M. M. Harris, L. C. Gavin, C. A. Murray, Y. Ortin, H. Müller-Bunz, C. J. Harding, Y. Lan, A. K. Powell and G. G. Morgan, Substituent Effects on Spin State in a Series of Mononuclear Manganese(III) Complexes with Hexadentate Schiff-Base Ligands, *Inorg. Chem.*, 2014, **53**, 6022–6033.

30 A. J. Fitzpatrick, E. Trzop, H. Müller-Bunz, M. M. Dîrtu, Y. Garcia, E. Collet and G. G. Morgan, Electronic vs. structural ordering in a manganese(III) spin crossover complex, *Chem. Commun.*, 2015, **51**, 17540–17543.

31 D. J. Harding, W. Phonsri, P. Harding, I. A. Gass, K. S. Murray, B. Moubaraki, J. D. Cashion, L. Liud and S. G. Telfer, Abrupt spin crossover in an iron(III) quinolylsalicylaldimine complex: structural insights and solvent effects, *Chem. Commun.*, 2013, **49**, 6340–6342.

32 W. Phonsri, D. J. Harding, P. Harding, K. S. Murray, B. Moubaraki, I. A. Gass, J. D. Cashion, G. N. L. Jameson and H. Adams, Stepped spin crossover in Fe(III) halogen substituted quinolylsalicylaldimine complexes, *Dalton Trans.*, 2014, **43**, 17509–17518.

33 K. Fukuroi, K. Takahashi, T. Mochida, T. Sakurai, H. Ohta, T. Yamamoto, Y. Einaga, H. Mori, K. Fukuroi, K. Takahashi, T. Mochida, T. Sakurai, H. Ohta, T. Yamamoto, Y. Einaga and H. Mori, Synergistic Spin Transition between Spin Crossover and Spin-Peierls-like Singlet Formation in the Halogen-Bonded Molecular Hybrid System: $[Fe(Iqsal)_2][Ni(dmit)_2]\cdot CH_3CN\cdot H_2O$, *Angew. Chem., Int. Ed.*, 2014, **53**, 1983–1986.

34 F. F. Martins, A. Joseph, H. P. Diogo, M. E. Minas da Piedade, L. P. Ferreira, M. D. Carvalho, S. Barroso, M. J. Romão, M. J. Calhorda and P. N. Martinho, Irreversible Magnetic Behaviour Caused by the Thermosalient Phenomenon in an Iron(III) Spin Crossover Complex, *Eur. J. Inorg. Chem.*, 2018, **2018**, 2976–2983.

35 A. I. Vicente, L. P. Ferreira, M. D. D. Carvalho, V. H. N. Rodrigues, M. M. Dîrtu, Y. Garcia, M. J. Calhorda and P. N. Martinho, Selecting the spin crossover profile with controlled crystallization of mononuclear Fe(III) polymorphs, *Dalton Trans.*, 2018, **47**, 7013–7019.

36 S. Ashoka Sahadevan, E. Cadoni, N. Monni, C. Sáenz De Pipaón, J. R. Galan Mascaros, A. Abhervé, N. Avarvari, L. Marchiò, M. Arca and M. L. Mercuri, Structural Diversity in a New Series of Halogenated Quinolyl Salicylaldimides-Based FeIII Complexes Showing Solid-State Halogen-Bonding/Halogen···Halogen Interactions, *Cryst. Growth Des.*, 2018, **18**, 4187–4199.

37 P. N. Martinho, A. I. Vicente, S. Realista, M. S. Saraiva, A. I. Melato, P. Brandão, L. P. Ferreira and M. d. D. Carvalho, Solution and solid state properties of Fe(III) complexes bearing N-ethyl-N-(2-aminoethyl)salicylaldiminate ligands, *J. Organomet. Chem.*, 2014, **760**, 48–54.

38 A. I. Vicente, A. Joseph, L. P. Ferreira, M. de Deus Carvalho, V. H. N. Rodrigues, M. Duttine, H. P. Diogo, M. E. Minas da Piedade, M. J. Calhorda and P. N. Martinho, Dynamic spin interchange in a tridentate Fe(III) Schiff-base compound, *Chem. Sci.*, 2016, **7**, 4251–4258.

39 R. T. Marques, F. F. Martins, D. F. Bekiş, A. I. Vicente, L. P. Ferreira, C. S. B. Gomes, S. Barroso, V. Kumar, Y. Garcia, N. A. G. Bandeira, M. J. Calhorda and P. N. Martinho, The Halogen Effect on the Magnetic Behaviour of Dimethylformamide Solvates in $[Fe(halide\text{-}salEen)_2]BPh_4$, *Magnetochemistry*, 2022, **8**, 162.

40 R. T. Marques, L. P. Ferreira, C. S. B. Gomes, C. S. D. Lopes, C. E. S. Bernardes, N. K. Sarangi, T. E. Keyes and P. N. Martinho, Reversible Single-Crystal-to-Single-Crystal Transformations in a salEen Fe(III) Spin Crossover Sponge, *Cryst. Growth Des.*, 2023, **23**, 3222–3229.

41 C. F. Sheu, S. M. Chen, G. H. Lee, Y. H. Liu, Y. S. Wen, J. J. Lee, Y. C. Chuang and Y. Wang, Structure and Magnetism of the Iron(III) Spin-Crossover Complex $[FeIII\{N\text{-}ethyl\text{-}N\text{-}(2\text{-}aminoethyl)salicylaldiminate\}_2]ClO_4$, *Eur. J. Inorg. Chem.*, 2013, **2013**, 894–901.

42 L. Krause, R. Herbst-Irmer, G. M. Sheldrick and D. Stalke, Comparison of silver and molybdenum microfocus X-ray sources for single-crystal structure determination, *J. Appl. Crystallogr.*, 2015, **48**, 3–10.

43 G. M. Sheldrick, Crystal structure refinement with SHELXL, *Acta Crystallogr., Sect. C: Struct. Chem.*, 2015, **71**, 3–8.

44 L. J. Farrugia, WinGX and ORTEP for Windows: an update, *J. Appl. Crystallogr.*, 2012, **45**, 849–854.

45 C. F. MacRae, I. Sovago, S. J. Cottrell, P. T. A. Galek, P. McCabe, E. Pidcock, M. Platings, G. P. Shields, J. S. Stevens, M. Towler and P. A. Wood, Mercury 4.0: from visualization to analysis, design and prediction, *J. Appl. Crystallogr.*, 2020, **53**, 226–235.

46 M. A. Spackman and D. Jayatilaka, Hirshfeld surface analysis, *CrystEngComm*, 2009, **11**, 19–32.

47 E. Milin, B. Benaicha, F. El Hajj, V. Patinec, S. Triki, M. Marchivie, C. J. Gómez-García and S. Pillet, Magnetic Bistability in Macrocycle-Based FeII Spin-Crossover Complexes: Counter Ion and Solvent Effects, *Eur. J. Inorg. Chem.*, 2016, **2016**, 5305–5314.

48 J. J. McKinnon, D. Jayatilaka and M. A. Spackman, Towards quantitative analysis of intermolecular interactions with Hirshfeld surfaces, *Chem. Commun.*, 2007, 3814–3816.

49 P. R. Spackman, M. J. Turner, J. J. McKinnon, S. K. Wolff, D. J. Grimwood, D. Jayatilaka and M. A. Spackman, CrystalExplorer: a program for Hirshfeld surface analysis, visualization and quantitative analysis of molecular crystals, *J. Appl. Crystallogr.*, 2021, **54**, 1006–1011.

50 M. A. Spackman and J. J. McKinnon, Fingerprinting intermolecular interactions in molecular crystals, *CrystEngComm*, 2002, **4**, 378–392.

51 A. Gil, M. Sodupe and J. Bertran, Unusual hydrogen bonds in $[AH_3\text{–}H_3O]^{\bullet+}$ radical cations (A = C, Si, Ge, Sn and Pb): Single-electron hydrogen bond, proton-hydride hydrogen bond and formation of $[H_2AOH_2]^{\bullet+}\text{–}H_2$ complexes, *Chem. Phys. Lett.*, 2004, **395**, 27–32.

52 A. Gil, A. Sanchez-Gonzalez and V. Branchadell, Unraveling the Modulation of the Activity in Drugs Based on Methylated Phenanthroline When Intercalating between DNA Base Pairs, *J. Chem. Inf. Model.*, 2019, **59**, 3989–3995.

53 S. Elleuchi, I. Ortiz De Luzuriaga, Á. Sanchez-Gonzalez, X. Lopez, K. Jarraya, M. J. Calhorda and A. Gil, Computational Studies on the Binding Preferences of Molybdenum(II) Phenanthroline Complexes with Duplex DNA. The Important Role of the Ancillary Ligands, *Inorg. Chem.*, 2020, **59**, 12711–12721.

54 Á. Sánchez-González and A. Gil, Elucidating the intercalation of methylated 1,10-phenanthroline with DNA: the important weight of the CH/H interactions and the selectivity of CH/π and CH/n interactions, *RSC Adv.*, 2021, **11**, 1553–1563.
55 Á. Sánchez-González, T. G. Castro, M. Melle-Franco and A. Gil, From groove binding to intercalation: unravelling the weak interactions and other factors modulating the modes of interaction between methylated phenanthroline-based drugs and duplex DNA, *Phys. Chem. Chem. Phys.*, 2021, **23**, 26680–26695.
56 R. Ketkaew, Y. Tantirungrotechai, P. Harding, G. Chastanet, P. Guionneau, M. Marchivie and D. J. Harding, OctaDist: a tool for calculating distortion parameters in spin crossover and coordination complexes, *Dalton Trans.*, 2021, **50**, 1086–1096.